Heriot-Watt University

Heriot-Watt University
Research Gateway

Gravity currents in rotating, wedge-shaped, adverse channels

Cuthbertson, Alan; Lundberg, P.; Davies, P. A.; Laanearu, J.

Published in:
Environmental Fluid Mechanics

DOI:
10.1007/s10652-013-9285-4

Publication date:
2014

Link to publication in Heriot-Watt Research Gateway

Citation for published version (APA):
Cuthbertson, A. J. S., Lundberg, P., Davies, P. A., & Laanearu, J. (2014). Gravity currents in rotating, wedge-shaped, adverse channels. Environmental Fluid Mechanics, 14(5), 1251-1273. 10.1007/s10652-013-9285-4

General rights
Copyright and moral rights for the publications made accessible in the public portal are retained by the authors and/or other copyright owners and it is a condition of accessing publications that users recognise and abide by the legal requirements associated with these rights.

If you believe that this document breaches copyright please contact us providing details, and we will remove access to the work immediately and investigate your claim.

GRAVITY CURRENTS IN ROTATING, WEDGE-SHAPED, ADVERSE CHANNELS

A. J. S. Cuthbertson[1,*], P. Lundberg[2], P. A. Davies[1], J. Laanearu[3]

[1] School of Engineering, Physics and Mathematics, University of Dundee, Dundee, DD1 4HN, UK. Email: a.cuthbertson@hw.ac.uk; p.a.davies@dundee.ac.uk

[2] Department of Meteorology/Oceanography, Stockholm University, SE10691, Sweden. Email: peter@misu.su.se

[3] Institute of Mechanics, Tallinn University of Technology, Ehitajate tee 5, 19086, Tallinn, Estonia. Email: janek.laanearu@ttu.ee

* Corresponding author: Current address – School of the Built Environment, Heriot Watt University, Edinburgh EH14 4AS, UK. Email: a.cuthbertson@hw.ac.uk. Phone: +44 131 451 8358. Fax: +44 131 451 4617.

ABSTRACT

Results are presented from a series of parametric experimental and analytical studies of the behaviour of dense gravity currents along rotating, up-sloping, wedge-shaped channels. High resolution density profile measurements at fixed cross- and along-channel locations reveal the outflowing bottom gravity currents to adjust to quasi-steady, geostrophically-balanced conditions along the channels, with the outflow layer thickness and cross-channel interface slope shown to scale with the inlet Burger number for all experimental conditions tested. A general analytical solution to the classic rotating hydraulics problem has been developed under the assumption of inviscid, zero-potential-vorticity conditions to model dense water flow through a triangular constriction and thus simulate the vee-channel configurations under consideration. Predictions from this zero-PV model are shown to provide good overall quantitative agreement with experimental measurements obtained both under hydraulically-controlled conditions at the channel exit and for subcritical conditions generated along the channel length. Quantitative discrepancies between measurements and analytical predictions are attributed primarily to assumptions and limitations associated with the zero-PV modelling approach adopted, as well as the to the rapid adjustment in outflow characteristics as the channel exit is approached, as characterised by the along-channel variation in densimetric Froude number for the outflows.

Keywords: Gravity currents; rotating flows; dense oceanic outflows; topographic control; zero potential vorticity assumption.

1. Introduction

The hydraulics of dense gravity current propagation along submarine channels in rotating systems have wide geophysical relevance, particularly in the marine environment where they play an important role in controlling buoyancy-driven exchanges in the open oceans, fjords and estuaries. For deep water oceanic outflows affected by the background rotation of the Earth, for example, topographical constraints imposed by the seafloor bathymetry (e.g. straits and sills) can control deep water exchange and exert significant influence on the internal velocity and density structure within the overflow. An example of such control occurs at the Faroe Bank Channel (FBC), where the Norwegian Sea Deep Water (NSDW) intrusion into the North Atlantic Ocean is topographically-constrained by the threshold sill at the entrance to the FBC (e.g. Østerhus *et al*., 1999; Duncan *et al*., 2003; Borenäs and Lundberg, 2004; Mauritzen *et al*., 2005; Girton *et al*., 2006). Fundamental knowledge of such topographic effects on the development and maintenance of geostrophic balance within constrained oceanic outflows (as indicated by the longitudinal and lateral variations of slope, distortion and elevation of the interface between the dense outflowing bottom layer and overlying, relatively-quiescent receiving waters) is relatively poorly understood. Additionally, the limiting and restricting effects of hydraulic control and transport capacity on the outflow behaviour remain to be fully explored.

A significant number of studies investigating such dense oceanic outflows within topographically-constrained submarine channels have adopted inviscid, rotating hydraulic modelling approaches (e.g. Whitehead *et al*., 1974; Borenäs and Lundberg, 1986; Pratt and Lundberg, 1991; Killworth, 1994) to predict deep-water transport in geophysically-relevant topographic situations (i.e. non-rectangular channels with a dynamically inactive upper layer). Such methods have been shown to generally demonstrate plausible predictions of measured

deep-water outflow transport rates (e.g. Borenäs and Lundberg, 1986; Laanearu and Lundberg, 2003). One aspect of these modelling techniques that remains to be resolved fully is their predictive capability for dense water outflows in topographically-constrained channels subject to hydraulic control (Girton *et al*., 2006; Sherwin *et al*., 2008).

A series of parametric experiments has thus been conducted within idealised, upwardly-sloping, uniform vee-shaped channels to investigate the dense water outflow characteristics outlined above. The experimental results have then been analysed in terms of predictions from an analytical model based on inviscid, rotating hydraulic theory to determine model sensitivity to (and predictive accuracy for) the dense water outflows generated within the channels.

2. The Physical System

Fig. 1(a) shows a schematic representation of the channel configuration under investigation, consisting of a vee-shaped channel with fixed side slope angle α (γ = tan α) and an along-channel adverse bed slope S_0, inclined upwards towards the channel exit. This configuration is considered an idealised topographic representation of a deep submarine channel, up-sloping in the longitudinal direction towards a submerged sill crest (Girton *et al*., 2006). The Cartesian coordinate system (x, y, z) is defined such that the x and y axes are orientated in the cross- and along-channel directions, respectively, while the positive z axis is taken as anti-parallel to the gravitational acceleration vector $\mathbf{g}$ = (0, 0, -g). Within the initial, undisturbed experiment configuration, the vee-shaped channel is submerged within a homogeneous ambient fluid of depth H and density ρ_0 and is in a state of solid body rotation with angular velocity $\mathbf{\Omega}$ = (0, 0, Ω) about the vertical z axis. At time t = 0, a dense water inflow of source density ρ_1 = [ρ_0 +

($\Delta\rho$)$_0$], kinematic viscosity ν and an initial volume flux Q_1 is introduced at the upstream end of the triangular channel via a near-bed inlet manifold.

2.1. Scaling Considerations

A dense water outflow along a submerged channel will be in geostrophic balance when the Coriolis acceleration due to background rotation balances the horizontal, cross-channel pressure gradient ($\partial p/\partial x$), i.e.

$$-fv = -\frac{1}{\rho_0}\frac{\partial p}{\partial x}, \tag{1}$$

where f (= 2Ω) is the Coriolis parameter and v is the along-channel component of outflow velocity. If pressure is assumed to be hydrostatic, Eq. (1) can be re-written as (Gill, 1982):

$$-fv = -\frac{g(\Delta\rho)_0}{\rho_0}\frac{d\eta}{dx} = -g'_0\gamma_g, \tag{2}$$

where $g'_0 = g(\Delta\rho)_0/\rho_0$ is the reduced gravitational acceleration for the outflowing dense water layer at the channel inlet; $(\Delta\rho)_0 = (\rho_1 - \rho_0)$ is the density difference between the outflowing and ambient fluids; γ_g (= tan α_g) is the cross-channel, geostrophically-adjusted interface slope and $\eta(x)$ is the interface elevation [Fig. 1(b)]. At the channel inlet, the dense water inflow has a triangular cross-section with typical horizontal and vertical dimensions l_0 and h_0, respectively [see Fig. 1(a)]. The subsequent evolution of the gravity current along the channel can then be described by (i) the outflow layer thickness $h(x,y)$, (ii) the cross-channel interface slope γ_i (= tan α_i) and (iii) the average along-channel velocity $v(y)$ [see Fig. 1(b)]. Under assumed conditions of no shear-induced mixing or entrainment between the outflowing dense water layer and overlying ambient fluid along the channel, the mean outflow velocity v_i at an arbitrary cross-section i can be estimated from $v_i = Q_1/A_i$, where cross-channel flow area A_i is determined from geometrical considerations [see Fig. 1(b)], such that:

$$A_i = \frac{h_{i,\max}^2}{2}\left(\frac{2\gamma}{\gamma^2 - \gamma_i^2}\right), \tag{3}$$

where $h_{i,\max}$ is the maximum outflowing layer thickness (i.e. at $x = 0$). Combining Eqs. (2) and (3) provides an implicit equation for the geostrophic balance in the cross-channel direction [i.e. by setting $\gamma_i = \gamma_g$ in Eq. (3)], which can then be solved iteratively for γ_g:

$$v_i = \frac{g_0' \gamma_g}{f} \approx \frac{2Q_1}{h_{i,\max}^2}\left(\frac{\gamma^2 - \gamma_g^2}{2\gamma}\right). \tag{4}$$

Thus, the dense water outflow observables [h_i, γ_i (α_i) and v_i] can be conveniently described in terms of (i) the inlet dimensions h_0 and l_0 [see Fig. 1(a)], (ii) the sidewall and along channel bed slopes γ and S_0 and (iii) the computed geostrophic slope γ_g and/or velocity v_g [i.e. from Eq. (2)]. In addition, the familiar non-dimensional parameters describing buoyancy-driven flows in rotating systems, *viz*.

$F_0 = v_0 / (g_0' h_0)^{1/2}$ the densimetric Froude number, (5)

$R_0 = v_0 / l_0 f$ the Rossby number, and (6)

$Bu_0 = (R_0 / F_0)^2$ the Burger number (7)

are also expected to have a dynamic role in the dense water outflow development. [For sufficiently high values of the Reynolds number Re_0 ($= \bar{v}_0 h_0 / \nu$), the dependence of the flow properties on Re_0 may be neglected; values in the experiments were typically in the range $Re_0 = O(10^2 - 10^3)$].

3. Experimental Arrangement

The experiments were conducted in a transparent-walled rectangular tank, fabricated from acrylic material, with overall dimensions of 2.5 m-long × 2.2 m-wide × 0.4 m-deep, mounted on a rotating table (Fig. 2). Two 2 m-long uniform vee-shaped channels with side slopes $\alpha =$

20° and 35° (γ = 0.364 and 0.700), respectively, were installed, in turn, within the tank with the along-channel bed slope S_0 = 0.0349 and 0.0524 (2° and 3°, respectively) inclined upwards towards the channel exit. With the minimum in-channel bed elevation $z_{b,min}$ = 0 at the upstream end of the channel [at the centreline, x = 0 – Fig. 1(b)], the corresponding minimum bed elevation at the downstream channel exit was thus $z_{b,min}$ = 70 mm and 105 mm for S_0 = 2° and 3°, respectively.

Prior to each experiment, the rectangular tank was filled with freshwater (ρ_0 = 998 kg.m^{-3}) to a total in-channel depth of 0.372 m, submerging the vee-channel channel topography. The turntable was then rotated from rest at a prescribed constant angular velocity Ω for period of several hours to ensure that spin-up to solid body rotation had been attained (van Heijst *et al*., 1990); values of Ω = 0.37 s^{-1} and 0.50 s^{-1} were used in the present study. At the start of each run, brine solution of constant density ρ_1 (ρ_1: 1005 and 1020 kg.m^{-3}) was pumped into the upstream end of the rotating channel via an inlet diffuser and manifold arrangement designed to (i) uniformly-distribute the inflow across the triangular channel and (ii) minimise mixing with the ambient fluid (Fig. 2). The corresponding reduced gravitational acceleration g'_0 associated with these brine inflows ranged from 0.068 to 0.212 m.s^{-2}. Volume flux Q_1 was increased incrementally at prescribed elapsed times during each experimental run, with a quasi-stationary dense water outflow layer allowed to develop along the adverse channel bottom for each Q_1 value. The initial inflow volume flux Q_1 was set at 0.167 l s^{-1} and was increased incrementally as Q_1 = 0.167 $\rightarrow$ 0.25 $\rightarrow$ 0.333 $\rightarrow$ 0.458 l s^{-1}. Parametric changes between runs were thus introduced by varying (i) the source volume flux Q_1 of the dense water overflow, (ii) the density difference $(\Delta\rho)_0 = (\rho_1 - \rho_0)$ between the dense brine and

ambient receiving waters, (iii) the background rotation rate Ω, and (iv) the vee-channel dimensions, defined by the cross- and along-channel bed slopes α and S_0 [see Fig. 1(a)].

It is noted that for all experimental conditions, the dense water outflow was contained completely within the vee-channel topography along its full length, before spilling out freely at the channel exit into the surrounding rectangular tank (via an open-pore block of reticulated foam to minimise mixing), from where it was removed by a gravity-driven siphon arrangement at the tank outlet (Fig. 2).

3.1 Experimental Measurements

The spatial and temporal development of the density field $\rho(x,y,z,t)$ was monitored at prescribed lateral channel cross-sections and centreline measurement locations in the along-channel direction (see Fig. 3 for details) using fixed arrays of high resolution, fast-response micro-conductivity probes (Head, 1983). The cross-channel measurements were preferentially positioned on right-hand side of the channel (looking downstream) to accommodate the expected adjustment in the outflow behaviour due to rotation effects, while centreline measurement locations were concentrated toward the downstream end of the channel (i.e. $y/L \rightarrow 1$) to record the longitudinal variation ($\partial/\partial y$) in the outflow layer thickness $h_i(x)$ as the channel exit is approached (see Fig. 3). The micro-conductivity probes were mounted on rigid support frames, each with a motorised rack system that enabled simultaneous and rapid profiling of the density field (Davies *et al*., 2006; Cuthbertson *et al*., 2004; 2006). The prescribed temporal resolution for these density profile measurements was set to 10 s, thus allowing the dynamic evolution of the dense outflowing layer to be monitored throughout the duration of each experimental run.

4. Experimental Results

4.1 Time-series density fields

Time series data derived from the sequential quasi-instantaneous density profiles, measured at prescribed locations along and across the channels (Fig. 3), describe the dynamic evolution of the dense outflowing bottom water layer throughout the experiment (i.e. for each incremental inflow volume flux Q_1 condition). These density profiles are plotted non-dimensionally as the density excess $\rho' = (\rho - \rho_0)/(\rho_1 - \rho_0)$ within the normalised time ($2\Omega t$) -space (z/H) domain. Figs. 4(a) and (b) present typical non-dimensional time-series density plots for a run with S_0 = 3°; α = 20° at the five upstream cross-channel stations [P1 – P5, y/L = 0.48, Fig. 3(a)] and four cross-channel stations close to the channel exit [P6 – P9, y/L = 0.97, Fig. 3(a)]. The vertical (dashed white) lines shown in Fig. 4 indicate prescribed non-dimensional times at which the inflow volume flux Q_1 was increased incrementally during the experimental run (i.e. $2\Omega t \approx$ 250, 500, 750). As indicated in Fig. 4, a well-defined, sharp pycnocline exists between the outflowing dense water layer ($\rho' \rightarrow 1$) and overlying ambient fluid ($\rho' = 0$) at all measurement stations where the dense bottom waters are detected [note: the dense water outflow layer is not detected at downstream stations P6 and P9, Fig. 4(b)]. This suggests that minimal turbulent mixing and entrainment is initiated between the two fluid layers during this experimental run, for which the Burger number Bu_0 (indicating the relative importance of stratification to rotation effects on the dense water outflow behaviour), ranges between Bu_0 = 0.18 and 0.21. This finding is in accord with the zero mixing assumption made in the scaling considerations (Section 2.1). Furthermore, the temporal development of the dense water outflow is also indicated by well-defined increases in layer thickness, following each prescribed increase in dense water volume flux Q_1, prior to the establishment of quasi-steady-state outflow conditions along the channel (see Section 4.4).

Fig. 5 shows similar time-series density plots for an experimental run with a lower Burger number range Bu_0 = 0.049 – 0.058 due to a lower initial reduced gravitational acceleration g'_0, and otherwise identical conditions to the run plotted in Fig. 4. Density profile measurements at probe locations P3 – P5 in Fig. 5(a) clearly indicate a more diffuse pycnocline between the outflowing layer and overlying ambient fluid, suggesting some degree of shear-induced interfacial mixing due to the diminished importance of stratification over rotation effects on the dense water outflow behaviour. It is noted, however, that there is no evidence of this diffuse pycnocline at the downstream probe locations [P6 – P9, Fig. 5(b)], suggesting that the density isopycnals must converge as the channel exit section is approached. This effect is discussed in greater detail in Section 4.3. Significant temporal fluctuations in the pycnocline elevation are also observed at all probe locations, with the adjustment to quasi-stationary outflow conditions along the channel following each incremental increase in Q_1 less obvious than for runs with higher Bu_0 values (i.e. where the relative influence of stratification is increased, Fig. 4).

The parametric influence of channel geometry (i.e. α and S_0) on interfacial mixing and/or temporal fluctuations in pycnocline elevation appears to be secondary compared with the effects of changes in volume flux Q_1, rotation rate f (= 2Ω) and the initial density excess $(\Delta\rho)_0$ (through g'_0). However, channel geometry will clearly influence the shape of the outflowing dense water layer along the channel [i.e. outflow layer thickness $h_i(x)$ and cross-channel interfacial slope α_i]. This parametric influence is discussed in detail in subsequent sections.

4.2 Cross-channel isopycnal variation

Figs. 6(a) and (b) show cross-channel variations in measured isopycnal elevations at y/L = 0.65 and 0.97 for runs in which the Burger numbers Bu_0 were 0.40 and 0.11, respectively.

Both figures indicate that the lateral inclination in isopycnals increases as the channel exit is approached (i.e. $y/L \rightarrow 1$), whilst vertical spacing between isopycnals is also shown to reduce in the along-channel direction. The effect of Bu_0 is observed by comparison of the $y/L = 0.65$ plots in Figs. 6(a) and (b), whereby the isopycnal separation is shown to be larger for the $Bu_0 = 0.40$ run [i.e. Fig. 6(b)], which is indicative of increased mixing at the interface between the dense outflow layer and overlying ambient fluid. Note: some evidence of "isopycnal pinching" at the left side of the outflow is also evident from the $y/L = 0.65$ plots, an effect that has been widely observed in the oceanic context [e.g. the Faroe Bank Channel overflow: Borenäs *et al.*, 2001; Hansen *et al.*, 2001 (Fig. 2)].

In order to define quantitatively the dense water outflow layer observables $h_i(x,y)$ and $\alpha_i(y)$ (see Fig. 1), the $\rho' = 0.2$ isopycnal was selected to represent the interface elevation between the outflowing dense water and overlying ambient fluid. The maximum outflow layer thickness $h_{i,\max}$ was therefore obtained directly from this $\rho' = 0.2$ elevation at the channel centreline (i.e. $x = 0$), while the interface slope γ_i (= tan α_i) was taken as the gradient of the best fit straight line through $\rho' = 0.2$ elevations measured laterally across the channel. Fig. 7 plots non-dimensionally the cross-channel (x/H) variation in the normalised interface elevation (z/H) for two runs conducted in the $\alpha = 20°$ channel (with $S_0 = 2°$), and Bu_0 values ranging from 0.40 – 0.49 [Fig. 7(a)] and 0.11 – 0.13 [Fig. 7(b)], respectively. Both Figs. 7(a) and (b) clearly indicate the expected increase in γ_i and reduction in $h_{i,\max}$ as the outflow converges and accelerates towards the channel exit (i.e. as $y/L = 0.65 \rightarrow 0.97$). Direct comparisons between Figs. 7(a) and (b) indicate that both $h_{i,\max}$ and γ_i increase as the Burger number Bu_0 reduces (i.e. as rotation effects on the outflow become relatively more important compared to stratification). This finding is in general accord with the scaling assumption of geostrophic balance within the developing dense water outflow [Eqs. (2) and (4), Section 2.1].

A similar parametric dependence of increasing γ_i values as the Burger number Bu_0 reduces (i.e. through an increase in the Coriolis parameter f for a constant g'_0 value) is demonstrated in the $\alpha = 35°$ channel at the downstream exit section (i.e. $y/L = 0.97$) (see Fig. 8). In addition, direct comparison of Figs. 6(a) and (b) also indicates that a reduction in the along-channel bed slope S_0 [0.0524 (3°) $\rightarrow$ 0.0349 (2°)] may also have the parametric influence of increasing γ_i through an increase in the mean outflow velocity v_i at the channel exit section (i.e. $y/L = 0.97$) within the less-adverse sloped channel. Both these findings are again in accord with the expected parametric dependences and scaling considerations for geostrophically-balanced outflow conditions developing along the channels.

In order to determine the degree to which dense water outflows have adjusted to geostrophically-balanced conditions along both vee-shaped channels, the predicted geostrophic slope γ_g can be computed iteratively from Eq. (4) for prescribed values of Q_1, g'_0, f and γ, and experimental measurements of the maximum outflow layer thickness $h_{i,\max}$. Figs. 9(a) and (b) compare computed geostrophic angles of interfacial inclination α_g (= arctan γ_g) with measured cross-channel interface inclination angles α_i (= arctan γ_i) at the different y/L measurement locations within the $\alpha = 20°$ and 35° channels (see Fig. 3), for the full range of Bu_0 values tested. Note: the associated error bars plotted on each dataset indicate the mean variation in α_i (and α_g) from the exact geostrophically-balanced condition $\alpha_i = \alpha_g$. For measurements within the $\alpha = 20°$ channel [Fig. 9(a)], good correlation is demonstrated between the α_i and α_g values (i.e. $\alpha_i = \alpha_g \pm 2°$) at $y/L = 0.48$, 0.65 and 0.97, indicating that the dense water outflow is generally adjusted to geostrophically-balanced conditions at all these measurement locations. Within the $\alpha = 35°$ channel [Fig. 9(b)], although the level of scatter

between measured α_i and computed α_g values is generally wider (i.e. $\alpha_i = \alpha_g \pm 3°$), the degree of correlation still indicates the outflow conditions to have also adjusted to geostrophically-balanced conditions at both $y/L = 0.62$ and 0.97 measurement locations.

As indicated previously in Figs. 7 and 8, γ_i (and γ_g) values are shown to increase in the along-channel direction due to the *convergence* of the dense water outflow layer as the downstream channel exit is approached ($y/L \rightarrow 1$). This flow convergence will be characterised by acceleration in the along-channel outflow velocity v_i, which in turn steepens the cross-channel interface γ_i and predicted geostrophic γ_g slopes [see Eq. (4)]. This outflow characteristic has been previously observed in oceanographic measurements (e.g. Girton *et al*, 2006) and large-scale experimental measurements (e.g. Cuthbertson *et al*., 2011) of topographically-constrained dense water overflows.

4.3 Along-channel isopycnal variation

Fig. 10 shows typical plots of the longitudinal variation in isopycnal elevations $\rho' = 0.1 – 0.9$ along the channel centreline (i.e. $x = 0$). In both cases, it is apparent that while the separation of the isopycnals varies along the channel, they are shown to converge as the channel exit is approached (i.e. $y/L \rightarrow 1$). This is representative of the strong isopycnal pinching that is often observed in regions of strong topographic constraint, where hydraulically-controlled ($F^2 = 1$) outflow conditions are attained (e.g. across the Faroe Bank Channel threshold sill, Girton *et al*., 2006). Measurements of the $\rho' = 0.2$ interface elevations were obtained to provide information on the longitudinal variation in the maximum outflow layer thickness $h_{i,\max}(y)$. Fig. 11 shows typical longitudinal interfacial profiles under quasi-stationary outflow conditions plotted for a range of parametric conditions (α, S_0 and Bu_0) in the non-dimensional domain y/L versus z/H. These profiles are shown to have a relatively shallow interface slope

in the upstream region of the channel ($y/L \leq$ ~0.6), which significantly steepens as the channel exit and "control section" (Girton *et al.*, 2006) is approached (i.e. $y/L \rightarrow 1.0$). The parametric dependence of these longitudinal profiles on Bu_0 is clearly shown for each individual plot in Fig. 11, whereby the effect of increasing Q_1 (hence increasing h_0 and therefore reducing Bu_0) results in an increased centreline layer thickness $h_{i,\max}$ along the channel. Direct comparison of Figs. 11(a) and (b) [and Figs. 11(e) and (f)] indicates that a decrease in Bu_0 (through a reduction in g'_0) will also increase the outflow layer thickness $h_{i,\max}$ along the channel, while the corresponding effect from increasing f appears to be minimal [from comparison of Figs. 11(a) and (c)]. In terms of effects of channel geometry, a reduction in longitudinal slope S_0 [Figs. 11(a) and (d)] and side-wall slope γ [Figs. 11(a) and (e)] are both shown to reduce the layer thickness $h_{i,\max}$, mainly due to the reduction in storage volume within the adverse-sloped channel and the associated increase in along-channel outflow velocities v_i that will be generated under these conditions.

4.4 Temporal adjustment in dense water outflow

It is informative to quantify the temporal adjustment of outflow layer thickness $h_{i,\max}$ in response to each prescribed increase in volume flux Q_1 during the experimental runs. Here, an outflow adjustment time t_a can be quantitatively defined as the time period, following the incremental increase in Q_1, for the outflow interface to adjust to its new quasi-stationary elevation at different along-channel locations. For practical purposes and consistency in the estimation of t_a, this elevation is assumed to be the 50^{th} percentile interface position following the increase in Q_1 (and prior to a subsequent increase). Within Fig. 12, these adjustment times are shown indicatively in non-dimensional time series ($2\Omega t$) plots of the normalised outflow layer thickness $h_{i,\max}/H$ obtained at each of the eight centreline y/L probe locations for the experimental conditions shown (Bu_0, S_0 and α). Comparing the plots in Fig. 12 for similar

channel geometries (i.e. α and S_0), it is apparent that the normalised adjustment times are generally shorter and less variable (i.e. mean: S.D in $2\Omega t_a$ = 53.3: 12.6 and 51.1: 12.1) for runs with higher Bu_0 values [see Figs. 12(a) and (c), respectively]. By contrast, within the lower Bu_0 runs (through lower g'_0 values), the normalised adjustment times were generally longer and more varied [i.e. mean: S.D in $2\Omega t_a$ = 60.2: 14.7 and 54.5: 13.5, Figs. 12(b) and (d), respectively]. This transient adjustment effect may be due to (i) lower outflow velocities v_i and/or (ii) adjustment to higher quasi-steady-state interface elevations (and associated increases in $h_{i,\max}$ layer thickness) along the channel for the lower Bu_0 runs (i.e. through the lower g'_0 values). This latter effect, in particular, implies that a larger in-channel *storage* volume is filled by the outflowing dense waters before quasi-steady-state overflow conditions are achieved. Note: the effect of channel inlet geometry (h_0, l_0) is also included through the Burger number Bu_0 as follows:

$$Bu_0 = \left(\frac{R_0}{F_0}\right)^2 = \left(\frac{g'_0 h_0}{f^2 l_0^2}\right) = k_1\left(\frac{g'_0}{f^2 h_0}\right), \tag{8}$$

where k_1 (= $\tan^2\alpha/4$) is a vee-channel shape factor relating inlet dimensions h_0 and l_0. Thus, values of Bu_0 increase with channel side slope γ (= $\tan\alpha$), although the overall parametric effects of γ and S_0 on $2\Omega t_a$ values are not clearly demonstrated within the data.

5. Analytical solution based on rotating hydraulics

Referring to the experimental arrangement described above, it is recognised that the inlet diffusor manifold fitted to the wedge-shaped channel served two purposes. Specifically, it minimized the initial mixing between the dense water inflow and the quiescent ambient fluid, as well as ensured that the potential vorticity of the working fluid initially was zero (hence mimicking the effects of an infinitely deep upstream reservoir). As each experiment proceeded, it was noted that the pycnocline separating the active dense bottom layer and the

ambient fluid generally remained very sharp along the channel, indicating limited or no interfacial mixing.

These observations imply that the active dense water outflow can be adequately described and characterized to the lowest order by inviscid zero-potential-vorticity conditions, *viz*. the framework of classic rotating hydraulics theory (Whitehead *et al*., 1974). Within the current configuration, the vee-channel bathymetry is prescribed as $z = z_b(x) = \gamma|x|$, where $\gamma = \tan\alpha$, as before. The interface separating the quiescent upper layer from the active dense water mass is assumed to be located at elevation $z = \eta(x)$ [Fig. 1(b)], with its upstream-reservoir level at η_∞. In accordance with Eq. (2), the along-channel velocity is taken to be geostrophically-balanced, with $fv(x) = g'\partial\eta/\partial x$, and the condition of zero-potential-vorticity flow becomes:

$$\frac{[f + \partial v(x)]}{\{\eta(x) - h(x)\}} = 0 \quad \Leftrightarrow \quad \frac{\partial v(x)}{\partial x} = -f \ . \tag{9}$$

Rescaling the equations using $x = (g'\eta_\infty)^{1/2} f^{-1} x^*$, $v = (g'\eta_\infty)^{1/2} v^*$ and $(h,\eta) = \eta_\infty (h^*, \eta^*)$, where x^*, v^*, and (h^*, η^*) are non-dimensional, we obtain $v^*(x^*) = \partial\eta^*/\partial x^*$ and $\partial v^*/\partial x^* = -1$. These two relationships yield a second-order O.D.E. for $\eta^*(x^*)$. In the subsequent analysis, the asterisks are dropped for convenience, while continuing to work in non-dimensional terms. Since the interface is taken to meet the left- and right-bank bathymetry at $x = -a$ and $x = b$ [Fig. 1(b)], respectively, the pertinent boundary conditions are $\eta(-a) = \mu a$ and $\eta(b) = \mu b$, where $\mu = \gamma(g'\eta_\infty)^{1/2}(f\eta_\infty)^{-1}$. The solution to this formal problem is thus:

$$\eta(x) = -\frac{x^2}{2} + C_1 x + C_2 ; \tag{10}$$

with $C_1 = \dfrac{(b-a)}{2} + \mu\dfrac{(b-a)}{(b+a)}$; $C_2 = \left(\dfrac{2\mu}{b+a} + \dfrac{1}{2}\right)ab$.

The non-dimensional transport Q is obtained by cross-channel integration [Fig. 1(b)], *viz*:

$$Q = \int_{-a}^{b} v(x)\{\eta(x) - h(x)\}dx = \frac{\mu^2}{2}(b^2 - a^2) + \frac{\mu}{3}(b^3 - a^3) - \frac{\mu}{2}\left\{\frac{\mu}{b+a} + \frac{1}{2}\right\}(b-a)(b^2 + a^2)\,. \quad (11)$$

In dimensional terms, Bernoulli's law can be written in the form: $v(x)^2 + 2g'\eta(x) = 2g'\eta_\infty$. This is most conveniently evaluated at $x = 0$, and assumes the non-dimensional form:

$$\mu^2 \frac{(b-a)^2}{(b+a)^2} + \frac{1}{4}(b+a)^2 + \mu(b+a) = 2\,. \quad (12)$$

Note that Eqs. (11) and (12) can be further rescaled non-dimensionally using the convenient substitution $(a,b) = \mu(a',b')$, such that:

$$\hat{Q} = \frac{Q}{\mu^4} = \frac{1}{2}(b'^2 - a'^2) + \frac{1}{3}(b'^3 - a'^3) - \frac{1}{4}(b'-a')(b'^2 + a'^2) - \frac{1}{2}\frac{(b'-a')(b'^2 + a'^2)}{b'+a'}\,, \quad (13)$$

$$\frac{(b'-a')^2}{(b'+a')^2} + \frac{1}{4}(b'+a')^2 + (b'+a') = \frac{2}{\mu^2}\,. \quad (14)$$

Using the Bernoulli equation [Eq. (14)] to eliminate $(b'-a')$ from Eq. (13), the following explicit result for the non-dimensional transport $\hat{Q}$ in terms of $(b'+a')$ is obtained:

$$\begin{aligned} 24\hat{Q} = \{&\frac{2}{\mu^2}(b'+a')^2 - (b'+a')^3 - \frac{1}{4}(b'+a')^4\}^{1/2}\{\frac{1}{4}(b'+a')^4 + \frac{5}{2}(b'+a')^3 + \\ &+ (9 - \frac{2}{\mu^2})(b'+a')^2 + (6 - 6\frac{2}{\mu^2})(b'+a')\}. \end{aligned} \quad (15)$$

The analysis is pursued on the basis of the outflow being hydraulically-controlled (i.e. internal critical flow conditions with densimetric Froude number $F = 1$). In order to utilize this condition, the following averaging procedure is introduced:

$$\langle \Phi(x) \rangle = \left(\int_{-a}^{b} \Phi(x)dx \right) / (b+a)\,, \quad (16)$$

and hereafter the following quantities are determined:

$$\langle v(x)\rangle = \mu\left(\frac{b-a}{b+a}\right), \tag{17}$$

$$\left\langle v(x)^2\right\rangle = \frac{1}{12}(b+a)^2 + \mu^2\left(\frac{b-a}{b+a}\right)^2, \tag{18}$$

$$\left\langle \eta(x) - \mu|x|\right\rangle = \frac{1}{12}(b+a)^2 + \frac{\mu}{4}(b+a) - \frac{\mu}{4}\frac{(b-a)^2}{b+a}. \tag{19}$$

Following Pratt and Whitehead (2007), the Froude number F can be expressed as follows:

$$F^2 = \frac{\langle v(x)\rangle^2}{\langle v(x)\rangle^2 - \left\langle v(x)^2\right\rangle + \left\langle \eta(x) - \mu|x|\right\rangle}, \tag{20}$$

which, based on the relationships derived above [Eqs. (17) – (19)], becomes

$$F^2 = \mu\frac{(b-a)^2}{(b+a)ab} = \frac{(b'-a')^2}{(b'+a')a'b'}. \tag{21}$$

Making use of the critical-flow condition, i.e. $F^2 = 1$, it is found that:

$$(b'-a')^2 = \frac{(b'+a')^3}{4+(b'+a')}. \tag{22}$$

Insertion of this expression into the Bernoulli equation [Eq. (14)], yields the following third-degree algebraic equation for $(b'+a')$:

$$(b'+a')^3 + 8(b'+a')^2 + \{20 - \frac{8}{\mu^2}\}(b'+a') - \frac{32}{\mu^2} = 0. \tag{23}$$

The discriminant Δ of this equation is:

$$\Delta = \frac{2^6}{3^3}(25 + 17\frac{2}{\mu^2} + 2\frac{4}{\mu^4} - \frac{8}{\mu^6}), \tag{24}$$

which is positive definite for $\mu > 0.595$. In this parametric regime, the cubic equation above [Eq. (23)] consequently has a unique real root associated with the critical-flow state (in

addition to a spurious pair of complex-conjugate roots). From this solution, the controlled transport can be calculated using the explicit formula for $\hat{Q}$ in terms of ($b' + a'$) [Eq. (15)]. In this respect, Fig. 13 shows the predicted relationships between scaling parameter μ, non-dimensional maximal transport rate $Q = \left(\hat{Q}.\mu^4\right)$ and ($b' + a'$) for the triangular constriction, as derived directly from Eqs. (23), (22) and (13), respectively.

It should be underlined that, in the present analysis, attention has been focused on critical-flow conditions ($F^2 = 1$). Note, however, that for a known transport rate Q, it is possible to determine the interface configuration $\eta(x)$ for any given value of the Froude number F. This is most conveniently done using the rescaled Bernoulli equation to determine a' in terms of an arbitrary b', *viz*. by solving the fourth-degree algebraic equation:

$$\frac{a'^4}{4} + \{b'+1\}a'^3 + \left\{\frac{3}{2}b'^2 + 3b' + 1 - \frac{2}{\mu^2}\right\}a'^2 + b'\left\{b'^2 + 3b' - 2 - \frac{4}{\mu^2}\right\}a' + \\ + b'^2\left\{\frac{b'^2}{4} + b' + 1 - \frac{2}{\mu^2}\right\} = 0 \qquad (25)$$

The discriminant $\Delta_q = I^3 - 27J^2$ of this equation is determined from:

$$I = b'^2 + b' - (1 - \frac{2}{\mu^2})^2/12\,, \qquad (26)$$

$$J = \frac{1}{48}\left\{\frac{6}{\mu^2}b'^3 - \left(\frac{10}{\mu^2} + 14\right)b'^2 + \left(\frac{8}{\mu^2} - 1\right)b' - \frac{2}{9}\left(1 - \frac{2}{\mu^2}\right)^3\right\}. \qquad (27)$$

When Δ_q is negative definite, Eq. (25) has two real and one pair of complex-conjugate roots. Each real value of b' thus corresponds to a subcritical as well as a supercritical solution to the hydraulic problem. Once this relationship has been ascertained (in the context of the current experiments for the larger "subcritical" value of a'), b' is varied until the pertinent value of

transport Q [Eq. (13)] is achieved. It should be noted that the value of μ, for which a subcritical solution to Eq. (25) can be found, also requires adjustment (through η_∞). Finally, reverting back to the original scaling, use can hereafter be made of the explicit formulation for $\eta(x)$ given in terms of a and b [Eq. (10)]. In this respect, Fig. 14 shows typical subcritical model solutions for the cross-channel interface profile over a range of μ and F values between 0.6 – 2.8 and 0.01 – 1.0, respectively. These are plotted non-dimensionally as $\eta(x)$ versus μx, which allows the influence of vee-channel geometry (i.e. $\gamma = \tan\alpha$) to be removed. It is interesting to note that many of the analytical solutions shown indicate return flow on the right hand side of the outflowing layer (i.e. at locations where the interfacial gradient $\partial\eta/\partial x$ is negative). Considering the plots shown in Fig. 14, it is apparent that the magnitude of this return flow is greater for smaller values of both μ [Fig. 14(b)] and F. The parametric relationship determining the conditions under which such bi-directional flow solutions are predicted is discussed in detail for the critical flow case ($F^2 = 1.0$) in Section 6 below.

6. Analytical Model Comparisons with Experimental Data

Direct comparisons were made between the measured experimental data and the analytical model predictions obtained from the zero-potential-vorticity (zero-PV) approach outlined above. A number of experimental runs were chosen for these comparisons, enabling the parametric influence of Q_1, g'_0, f, α and S_0 on model predictions to be investigated using the analytical procedure described in Section 5. For these experimental-analytical comparisons, it is implicitly assumed that critical flow conditions ($F^2 = 1.0$) exist at the downstream cross-channel measurement section ($y/L = 0.97$), with maximal transport Q set equal to the initial volume flux Q_1 (i.e. no interfacial mixing or entrainment along the channel is accounted for). The zero-PV approach was utilised to predict the cross-channel interface elevation $\eta(x)$ and slope α_i through the explicit solution of Eq. (23) for $(b' + a')$ (i.e. for known values of μ) and

subsequently ($b' - a'$) from Eq. (22), whilst ensuring that the appropriate dimensionless maximal transport condition Q is satisfied through Eq. (13). Converting the resulting b' and a' values back to the original scaling through $(a',b') = \mu(a,b)$, the normalised cross-channel interface profile $\eta(x)$ for the zero-PV solution can then be obtained by back-substitution of positions b and a into Eq. (10). This profile can then made dimensional by applying the scaling terms for x and η, defined previously.

Fig. 15 shows typical dimensional comparisons between measured $\rho' = 0.2$ interface elevations at the downstream channel exit section ($y/L = 0.97$) and predicted interfacial elevations $\eta(x)$. In general, good quantitative agreement is demonstrated between the experimental data and zero-PV model predictions. Specifically, the predictions demonstrate the same parametric dependence on the independent experimental variables (i.e. Q_1, g'_0, f, α, S_0), in accord with the assumption of geostrophic-balance within the outflow. Quantitative discrepancies between measurements and predictions can generally be attributed either to (i) neglect of any interfacial mixing and/or entrainment effects (which will increase Q and/or reduce g' along the channel), (ii) the assumption of quasi-stationary conditions being established within the channel (i.e. ignoring temporal variability in the interface elevation – see Fig. 5), (iii) the implicit assumption of critical flow conditions at the downstream cross-channel measurement section (i.e. $y/L = 0.97$), and (iii) the arbitrary selection of the *representative* isopycnal $\rho' = 0.2$ for the density interface.

It is again interesting to note that the zero-PV predictions in Fig. 15(b) indicate return flows to occur at the right hand edge of the outflow layer, characterised by the interface gradient $\partial\eta/\partial x < 0$. From differentiation of Eq. (10), it is known that $\partial\eta/\partial x = v(x) = C_1 - x$, and hence it is

recognized that the lowest along-channel velocities will be found adjacent to the right bank of the vee-shaped channel, *viz*. at $x = b$. If a flow reversal is to occur over the control section for changing values of the parameter μ, it will consequently first manifest itself in the form of $v(b) = C_1 - b = 0$ for μ_c. Substituting for C_1, this condition yields $(b + a)^2 = 2\mu_c(b - a)$, thereafter use of this result in the criterion $F^2 = 1.0$ [Eq. (21)] ultimately leads to $(b + a) = 2\mu_c(\sqrt{2} - 1)$. By applying the same condition in the non-dimensional Bernoulli equation [Eq. (12)], the alternative result: $(b + a) = \sqrt{\mu_c^2 + 4} - \mu_c$ is obtained. Equating these two expressions for $(b + a)$ yields the following critical value of μ delimiting the bi- and uni-directional controlled-flow regimes:

$$\mu_c^2 = \frac{1}{2 - \sqrt{2}} \;\Rightarrow\; \mu_c \approx 1.31. \tag{28}$$

Previous investigations (e.g. Borenäs and Lundberg 1986, 1988) have established that wide passages are conducive to the establishment of bi-directional critical flow. Since the parameter μ is directly proportional to the "bathymetric" parameter γ (which, in turn, is inversely proportional to the passage width), it is recognized that for $\mu > 1.31$ the controlled, and hence maximal, transport takes place without any flow reversals. For the experimental runs shown in Fig. 14, the values of μ vary between (a) 1.84 – 2.32; (b) 0.88 – 1.07; (c) 2.20 – 2.82; and (d) 2.27 – 2.90, respectively. Hence, for the runs shown in Fig. 15(b) the values of μ are significantly lower than the critical values and, the zero-PV solutions suggest that bi-directional critical flow will be established under these conditions. It should be noted, however, that the experimental configuration of the density probes and their spatial cross-channel resolution [see Fig. 15(b)] precluded the detection of any bi-directional flow close to the right-hand boundary of the outflowing layer for any of these cases.

Cross-channel interfacial inclination angles α_i were estimated from the gradient of the predicted cross-channel profiles $\eta(x)$ at $x = 0$ and are compared directly with measured α_i values in Fig. 16. In general, this comparison again shows reasonably good quantitative agreement (generally within ± 3°), with only the data corresponding to Fig. 15(b) runs showing significant quantitative discrepancies, again attributed to the reasons outlined above.

As indicated previously (Section 5), the Zero-PV analytical model can also be employed to determine cross-channel interface profiles $\eta(x)$ for any value of F when the transport rate Q is known [i.e. through explicit solution of Eqs. (13), (25) and (10)] (see Fig. 14). From such subcritical analytical model predictions, and with knowledge of the vee-channel geometry and slope (i.e. γ and S_0), it is therefore possible to estimate the longitudinal variation in the upstream reservoir level η_∞ relative to the local minimum bed elevation $z_{b,\min}$ and, hence, obtain a prediction of the change in outflow interface shape along the channel (see Fig. 17). These predicted interface "surfaces" can be compared directly with the measured cross- (red data) and along-channel (green data) interface elevations obtained at locations within the vee-channel at which the conductivity probes were sited (see Fig. 3). Overall, the level of quantitative agreement between the discrete experimental measurements and analytical predictions is good in both the lateral cross-sections (i.e. at y/L = 0.65 and 0.97) and at longitudinal measurement positions along the channel centreline (i.e. $x/L = 0$). However, some discrepancies are observed, particularly in the former case when the predicted outflow conditions are bi-directional in nature [i.e. at y = 0.7 m, Fig. 17(b)], and, in the latter case, experimental-analytical divergence occurs towards the downstream channel exit [i.e. $y \rightarrow 0$, Fig. 17(a)-(c)]. This divergence may be at least partly explained by the predicted variation in Froude number F along the channel (Fig. 18), which reveals a rapid increase in F values for the outflow layer as the channel exit is approached (i.e. $y/L \rightarrow 1$). This effect has been

observed within an oceanographic context for the dense water overflow across the Faroe Bank Channel threshold sill (e.g. Fig. 7, Girton *et al*., 2006) and indicates that: (i) the assumption of critical flow conditions (F = 1.0) at the downstream cross-channel measurement section may be a significant overestimate [from Fig. 18, $F \approx 0.5$ (i.e. subcritical) at y/L = 0.97]; and (ii) experimental-analytical variability in cross-channel interface profiles $\eta(x)$ (Fig. 14) and slopes γ_i (Fig. 15) may result from significant sensitivity to changes in these local F values as the channel exit is approached.

6. Discussion and Concluding Remarks

The study has demonstrated that both qualitative and quantitative aspects of the hydraulic behaviour of dense bottom gravity currents within rotating systems are captured well by the analytical model based upon inviscid, rotating hydraulics theory and adoption of the simple zero-potential vorticity assumption (i.e. zero-PV model). Specifically, the application of this zero-PV approach to inclined, topographically-constrained, vee-channel geometries for critical flow conditions (F^2 = 1.0) has been demonstrated to generally predict well both the cross-channel variation in interfacial layer elevations η and the interface inclinations γ_i at the exit section to the channel. Parametric dependences, consistent with geostrophically-balanced outflows, are also clearly demonstrated in both the experimental measurements and analytical predictions. Broadening the application of the zero-PV model to subcritical predictions ($F^2 <$ 1) within the upstream channel, for a known transport rate Q, also demonstrates good agreement with both cross- and along-channel interface observations.

In all cases, quantitative discrepancies are largest for experimental conditions in which bi-directional flows are predicted by the zero-PV approach along the vee-channel section. It is worth noting here that these particular bi-directional flow situations may be a direct

consequence of the zero potential vorticity assumption itself and such flow reversals may not be a feature of equivalent non-zero or constant potential vorticity analytical solutions under the same experimental conditions. No evidence of these bi-directional outflow conditions was identified in the cross-channel experimental measurements, most likely due to the positioning and resolution of conductivity probes at the chosen cross-channel measurement sections [particularly at the right-hand boundary of the outflowing layer – see Fig. 15(b)]. Another reason for quantitative discrepancies between experimental measurements and analytical predictions is due to the rapid longitudinal variation ($\partial/\partial y$) in the outflow layer geometry (i.e. η and γ_i), and its sensitivity to the local Froude number F, as the channel exit section is approached ($y/L \rightarrow 1$).

Furthermore, well-established limitations of classic rotating hydraulics theory, either with the adoption of zero or constant (non-zero) potential vorticity, include the assumptions of (i) inviscid fluid conditions at the channel boundaries and interface between the dense gravity current and the overlying, less dense ambient receiving waters, and (ii) the exclusion of mixing and/or entrainment between the outflowing dense water and the overlying, relatively-quiescent, ambient receiving waters. Consideration of these effects is beyond the scope of this current paper. It is acknowledged, however, that although the majority of laboratory data presented here indicated shear-induced entrainment and turbulent mixing across the density interface to be limited [and restricted to a small number of experimental cases, e.g. Fig. 4(a)], previous related large-scale laboratory experimental studies (Cuthbertson *et al.*, 2011) and field measurements (e.g. Sherwin and Turrell, 2005; Sherwin *et al*., 2008) have indicated this interfacial mixing and entrainment to be a common feature of topographically-constrained oceanic outflows. Quantitative discrepancies between the predictions of this simple zero-PV rotational hydraulic approach and field observations for these cases are therefore anticipated.

However, these quantitative differences should not detract from the clear demonstration that the essential dynamics and physical (qualitative) description of the topographically-constrained outflows should be well represented by the application of classical rotating hydraulics in the zero potential vorticity assumption.

Acknowledgements

This work was supported by the Natural Environment Research Council (NERC) under the Strategic Ocean Funding Initiative (SOFI) programme. Collaborative research between Heriot-Watt, Dundee, Stockholm and Tallinn was supported through a Royal Society of Edinburgh International Exchange grant awarded to AJSC and a Distinguished Visiting Fellowship awarded to JL from The Royal Academy of Engineering (UK) tenable at the University of Dundee.

References

Borenäs, K. and P. Lundberg (1986). Rotating hydraulics of flow in a parabolic channel. *J. Fluid Mech.*, 167, pp 309 – 326.

Borenäs, K. and P. Lundberg (1988). On the deep-water flow through the Faroe Bank Channel. *J. Geophys. Res.*, 93(C2), pp 1281 – 1292.

Borenäs, K., Lake, I. L. and P. Lundberg (2001). On the Intermediate Water Masses of the Faroe–Bank Channel Overflow. *Journal of Physical Oceanography*, 31, 1904 – 1914.

Borenäs, K. and P. Lundberg (2004). The Faroe-Bank Channel deep-water overflow. *Deep-Sea Research Part II*, 51, 335-350.

Cuthbertson, A. J. S., P. A. Davies, M. J. Coates and Y. Guo (2004). A modelling study of transient, buoyancy-driven exchange flow over a descending barrier. *Environmental Fluid Mechanics*, 4, 127-155.

Cuthbertson, A. J. S., P. A. Davies and Y. Guo (2006). Model study of the influence of submerged tidal barriers on estuarine mixing and exchange processes. *ASCE J. Hydraulic Engineering*, 132(10), 1033-1043.

Cuthbertson, A. J. S., Laanearu, J., Wåhlin, A. K. and Davies, P. A. (2011). Experimental and analytical investigation of dense gravity currents in a rotating, up-sloping and converging channel. Dynamics of Atmospheres and Oceans, 52(3), 386-409.

Duncan, L. M., H. L. Bryden and S. A. Cunningham (2003). Friction and mixing in the Faroe Bank Channel outflow. *Oceanol. Acta*, 26 (5-6), 473-486.

Davies, P. A., A. Wåhlin and Y. Guo (2006). A combined laboratory and analytical study of flow through the Faroe Bank Channel, *J. Physical Oceanography*, 36 (7), 1348-1364.

Hansen, B., Turrell, W. R. and Østerhus, S. (2001). Decreasing overflow from the Nordic Seas into the Atlantic Ocean through the Faroe Bank Channel since 1950. *Nature*, 411, 927 – 930.

Gill, A. E. (1982). Atmosphere-Ocean Dynamics. Academic Press, San Diego.

Girton, J. B., L. J. Pratt, D. A. Sutherland and J. F. Price (2006). Is the Faroe Bank Channel overflow hydraulically controlled? *J. Physical Oceanography*, 36, 2340-2349.

Head, M. J. (1983). The use of four electrode conductivity probes for high resolution measurement of turbulent density or temperature variation in salt-stratified water flows. Ph.D. dissertation, University of California, San Diego, 242 pp.

Killworth, P.D. (1994). On reduced-gravity flow through sills. *Geophys. Astrophys. Fluid Dyn.*, 75, 91–106.

Laanearu, J., Lundberg, P. (2003). Topographically constrained deep-water flows in the Baltic Sea. *Journal of Sea Research*, 49 (4), 257–265.

Mauritzen, C., J. Price, T. Sanford and D. Torres (2005). Circulation and mixing in the Faroese Channels. *Deep-Sea Research Part I*, 52, 883-913.

Østerhus, S., B. Hansen, R. Kristiansen and P. Lundberg (1999). The overflow through the Faroe Bank Channel, *International WOCE Newsletter*, Vol. 25, WOCE International Project Office, Southampton, United Kingdom, 35-37.

Pratt, L.J. and Lundberg, P.A. (1991). Hydraulics of rotating strait and sill flow. *Ann. Rev. Fluid Mech. 23*, 81–106.

Pratt, L.J. and J.A. Whitehead (2007). Rotating Hydraulics: Nonlinear Topographic Effects in the Ocean and Atmosphere. Springer Science + Business Media, LLC, New York.

Sherwin, T. J. and W. R. Turrell (2005). Mixing and advection of a cold water cascade over the Wyville Thomson Ridge. *Deep-Sea Research Part I*, 52, 1392-1413.

Sherwin, T. J., C. R. Griffiths, M. E. Inall and W. R. Turrell (2008). Quantifying the overflow across the Wyville Thomson Ridge into the Rockall rough. *Deep-Sea Research Part I*, 55, 396-404.

van Heijst, G. J. F., P.A. Davies and R. G. Davis (1990). Spin up in a rectangular container. *Phys. Fluids*, A2, 150-159.

Whitehead, J .A., Leetmaa, A. and Knox, R. A. (1974). Rotating Hydraulics of Strait and Sill Flows. *Geophysical and Astrophysical Fluid Dynamics*, 6(2), 101 - 125.

Figure Captions

Fig. 1: Schematic representations of (a) dense water outflow characteristics along channel and main experimental parameters, and (b) typical cross-channel variations in outflow observables and channel dimensions.

Fig. 2: Schematic representation of the experimental set-up showing inlet and outlet conditions.

Fig. 3: Plan view of vee-channels showing typical cross-channel (red) and longitudinal (blue) micro-conductivity probe measurement stations within (a) $\alpha = 20°$ and (b) $\alpha = 35°$ channels.

Fig. 4: Non-dimensional time series plots of density fields at cross-channel measurement stations (a) P1 – P5, $y/L = 0.48$ and (b) P6 – P9, $y/L = 0.97$ [Fig. 3(a)] for run with g'_0: f: α: S_0 = 0.212 m.s^{-2}: 0.499 s^{-1}: 20°: 3°.

Fig. 5: Caption as for Fig. 4 with g'_0: f: α: S_0 = 0.068 m.s^{-2}: 0.497 s^{-1}: 20°: 3°.

Fig. 6: Cross-channel variation in isopycnal ρ' elevations at $y/L = 0.65$ and 0.97 for runs with Burger number Bu_0 = (a) 0.40 and (b) 0.11.

Fig. 7: Non-dimensional plots of cross-channel interface slope at y/L positions shown for runs with Bu_0 values of (a) 0.486 (blue); 0.452 (red); 0.429 (green); 0.400 (yellow), and (b) 0.130 (blue); 0.124 (red); 0.115 (green); 0.107 (yellow). Note: bed slopes $\alpha = 20°$ and $S_0 = 2°$ in all plots.

Fig. 8: Non-dimensional plots of cross-channel interface slope at y/L positions shown for runs with S_0: Bu_0 values of (a) 3°: 0.668 (blue); 0.612 (red); 0.589 (green); 0.549 (yellow), and (b) 2°: 0.451 (blue); 0.413 (red); 0.390 (green); 0.362 (yellow). Note: bed slope $\alpha = 35°$ in both plots.

Fig. 9: Comparison of measured cross-channel interface inclination angles α_i and predicted geostrophic inclination angles α_g [from Eqn. (4)] for (a) $\alpha = 20°$ and (b) $\alpha = 35°$ channel.

Fig. 10: Along-channel variation in isopycnal ρ' elevations at the channel centreline ($x = 0$) for runs with Burger number Bu_0 = (a) 0.40 and (b) 0.11.

Fig. 11: Longitudinal $\rho' = 0.2$ isopycnal elevation profiles along channel centreline ($x = 0$) for runs with α: S_0: Bu_0 values of: (a) 20°: 3°: 0.361 → 0.321 [green → blue], (b) 20°: 3°: 0.114 → 0.096, (c) 20°: 3°: 0.208 → 0.184, (d) 20°: 2°: 0.486 → 0.400, (e) 35°: 3°: 1.299 → 1.092, and (f) 35°: 3°: 0.377 → 0.309.

Fig. 12: Normalised centreline outflow layer thickness $h_{i,\max}/H$ versus normalised time $2\Omega t$ for runs with α: S_0: Bu_0 values of (a) 20°: 2°: 0.486 → 0.400, (b) 20°: 2°: 0.233 → 0.199, (c) 35°: 3°: 1.299 → 1.092, and (d) 35°: 3°: 0.668 → 0.549, at y/L probe locations shown.

Fig. 13: Comparison of non-dimensional analytical relationships between (a) scaling parameter $\mu = \alpha(g'\eta_\infty)^{1/2}(f\eta_\infty)^{-1}$ and (b) maximal transport rate Q with normalised outflow layer width ($b' + a'$) [derived from Eqs. (23) and (15), respectively].

Fig. 14: Analytical model solutions of normalised cross-channel interface profiles $\eta(x)$ versus μx for subcritical flow conditions ($F = 0.01 – 1.0$) and μ values in the range (a) 1.28 – 1.84, (b) 0.60 – 0.87, and (c) 1.96 – 2.79.

Fig. 15: Cross-channel variation in $\rho' = 0.2$ interface elevations at $y/L = 0.97$ (data points) with $\eta(x)$ predictions from zero-PV model (solid lines) for g'_0: f: α: S_0 values of (a) 0.212: 0.370: 20: 2.0, (b) 0.068: 0.370: 20: 2.0, (c) 0.117: 0.367: 35: 3.0 and (d) 0.121: 0.496: 35: 2.0. Volume flux Q_1 = 0.167 $l.s^{-1}$ (blue); 0.25 $l.s^{-1}$ (red); 0.330 $l.s^{-1}$ (green) and 0.458 $l.s^{-1}$ (yellow).

Fig 16: Comparison of experimental measurements and zero-PV predictions of cross-channel interface slopes α_i at $x = 0$ for experimental runs detailed in Fig. 13. Dashed lines show $\alpha_{i,meas} = \alpha_{i,zero\text{-}PV} \pm 2.5°$.

Fig. 17: Three-dimensional representations of zero-PV model predictions of dense outflow layer development along adverse-sloped channel for runs with μ values of (a) 1.27–1.84; (b) 0.60–0.87; and (c) 1.96–2.79. Corresponding cross-channel (red data) and centreline (green data) interface elevation measurements shown for comparison.

Fig. 18: Longitudinal variation in the predicted outflow Froude number F for runs with μ values of (a) 1.27–1.84; (b) 0.60–0.87; and (c) 1.96–2.79.

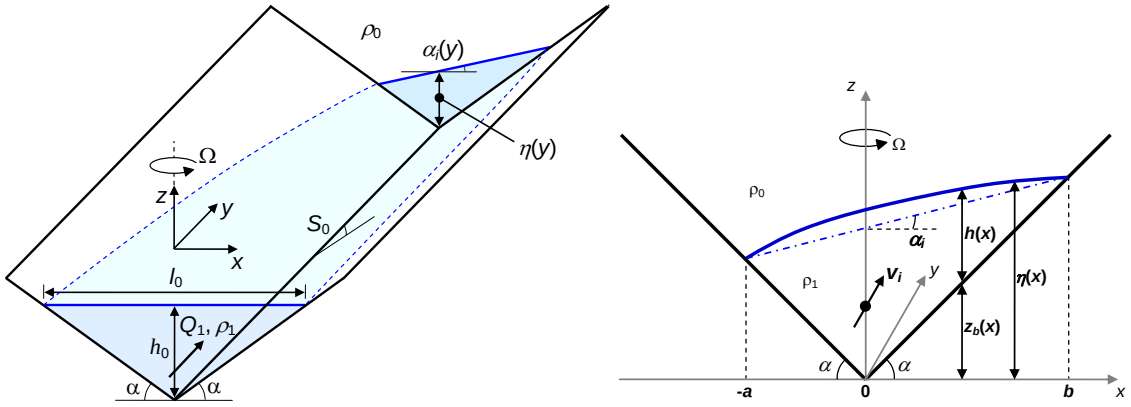

(a) **(b)**

Figure 1

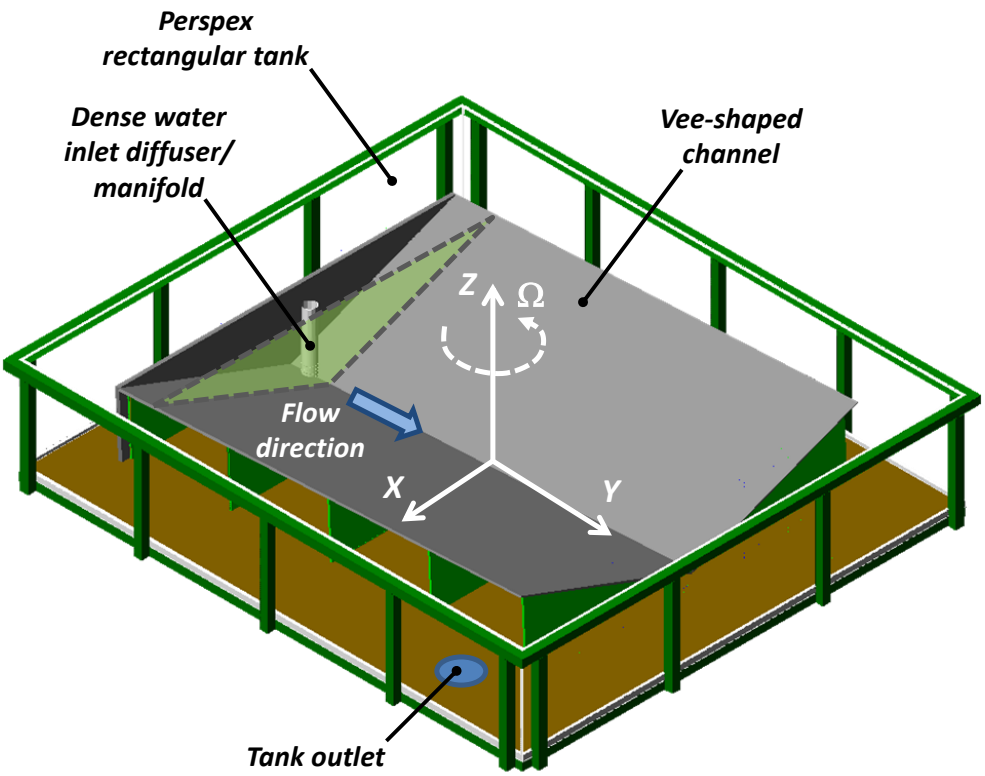
Perspex
rectangular tank
Dense water
inlet diffuser/
manifold
Vee-shaped
channel
Z
Ω
Flow
direction
X
Y
Tank outlet

Figure 2

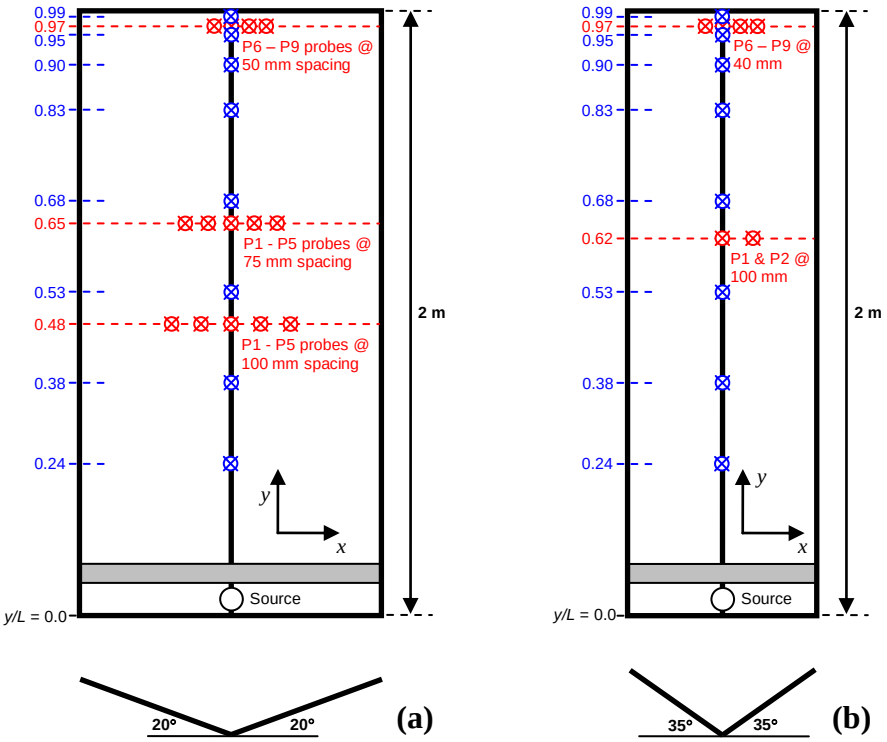
0.99
0.97
0.95
0.90
0.83
0.68
0.65
0.53
0.48
0.38
0.24
P6 – P9 probes @
50 mm spacing
P1 - P5 probes @
75 mm spacing
P1 - P5 probes @
100 mm spacing
2 m
y
x
Source
y/L = 0.0
20°
20°
(a)
0.99
0.97
0.95
0.90
0.83
0.68
0.62
0.53
0.38
0.24
P6 – P9 @
40 mm
P1 & P2 @
100 mm
2 m
y
x
Source
y/L = 0.0
35°
35°
(b)

Figure 3

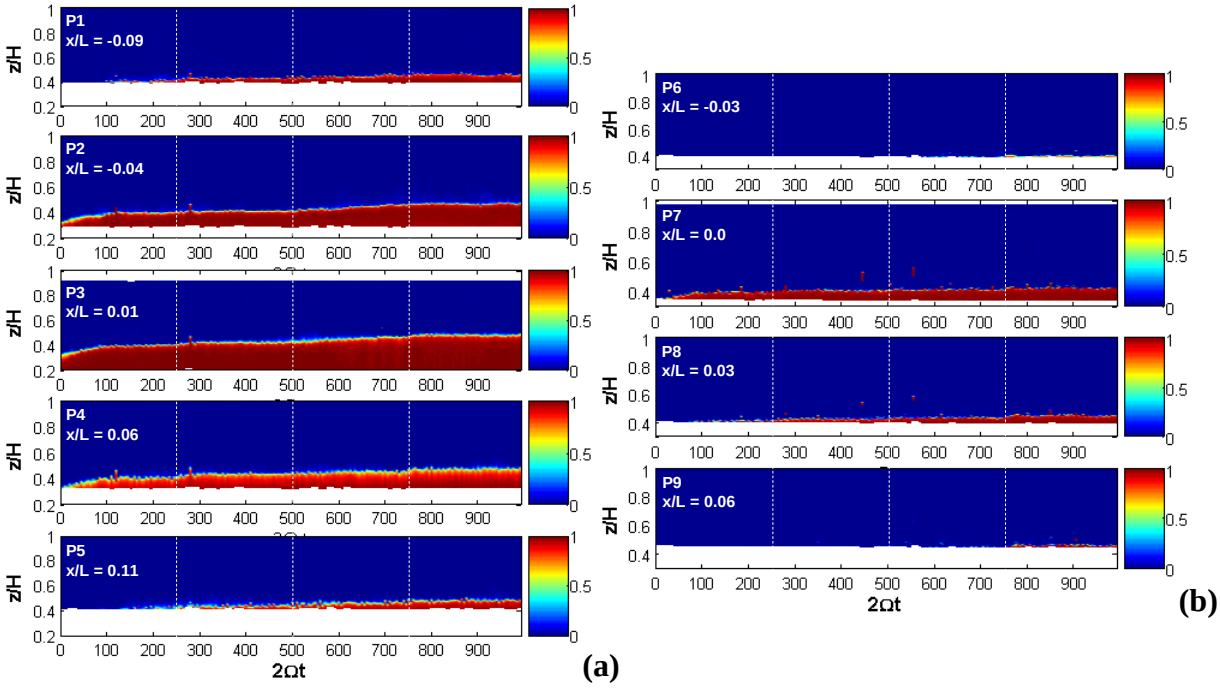
P1
x/L = -0.09
P2
x/L = -0.04
P3
x/L = 0.01
P4
x/L = 0.06
P5
x/L = 0.11
P6
x/L = -0.03
P7
x/L = 0.0
P8
x/L = 0.03
P9
x/L = 0.06
z/H
2Ωt
(a)
(b)

Figure 4

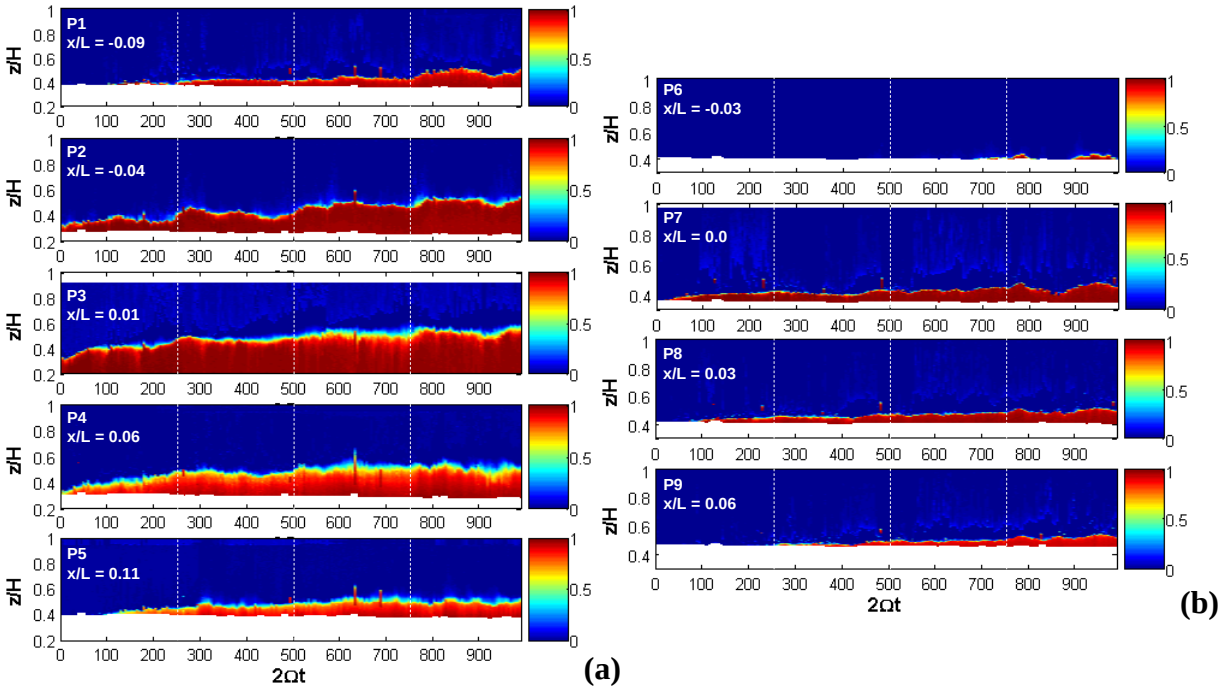
P1
x/L = -0.09
P2
x/L = -0.04
P3
x/L = 0.01
P4
x/L = 0.06
P5
x/L = 0.11
P6
x/L = -0.03
P7
x/L = 0.0
P8
x/L = 0.03
P9
x/L = 0.06
z/H
2Ωt
(a)
(b)

Figure 5

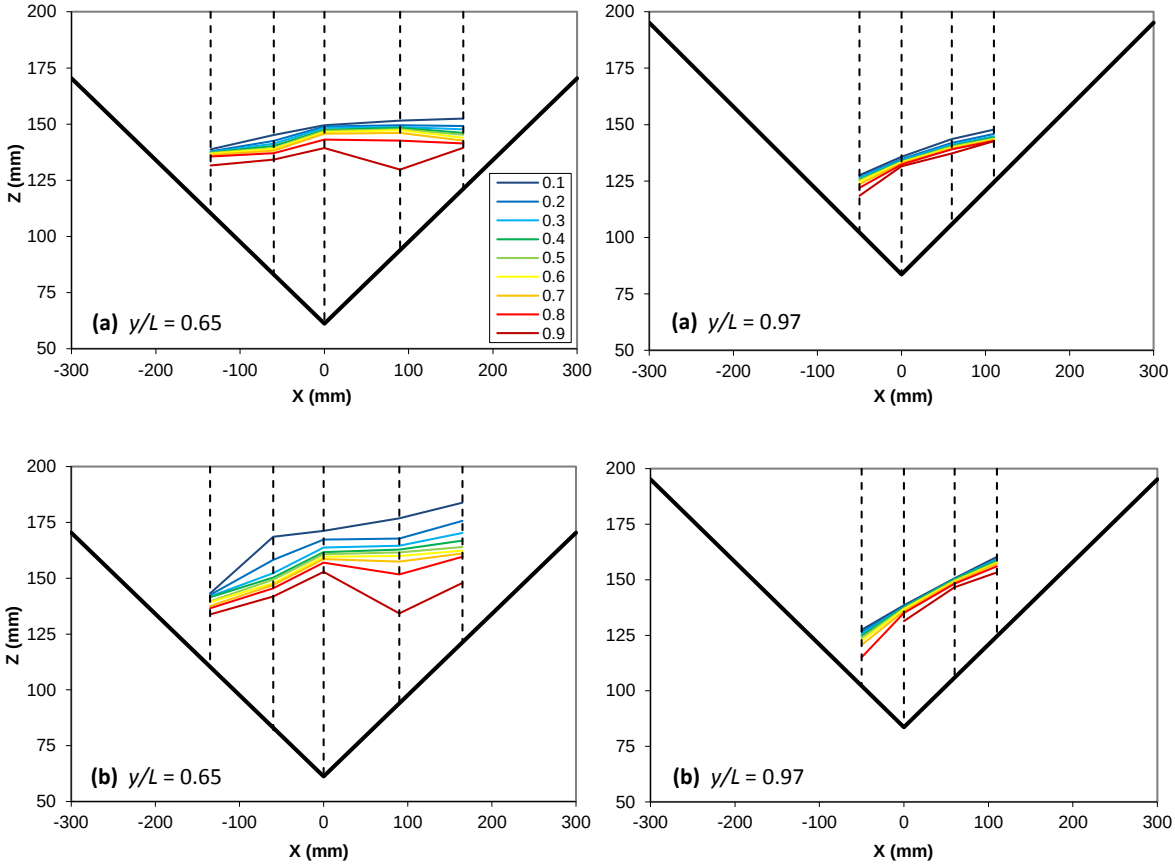

Figure 6

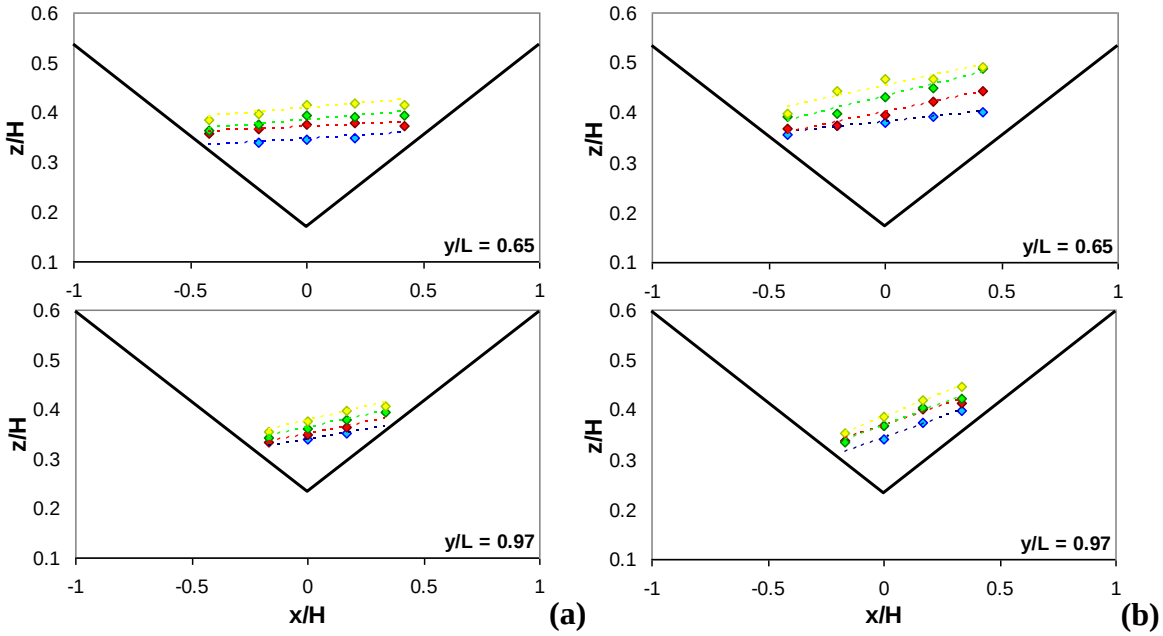

Figure 7

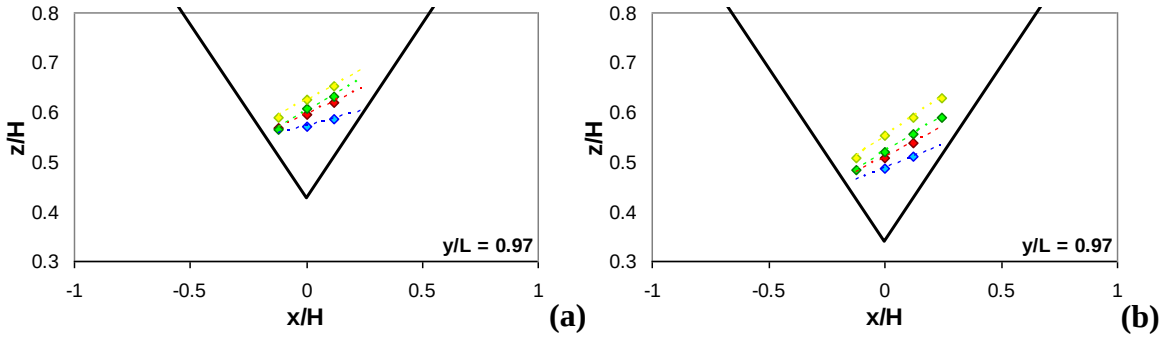

Figure 8

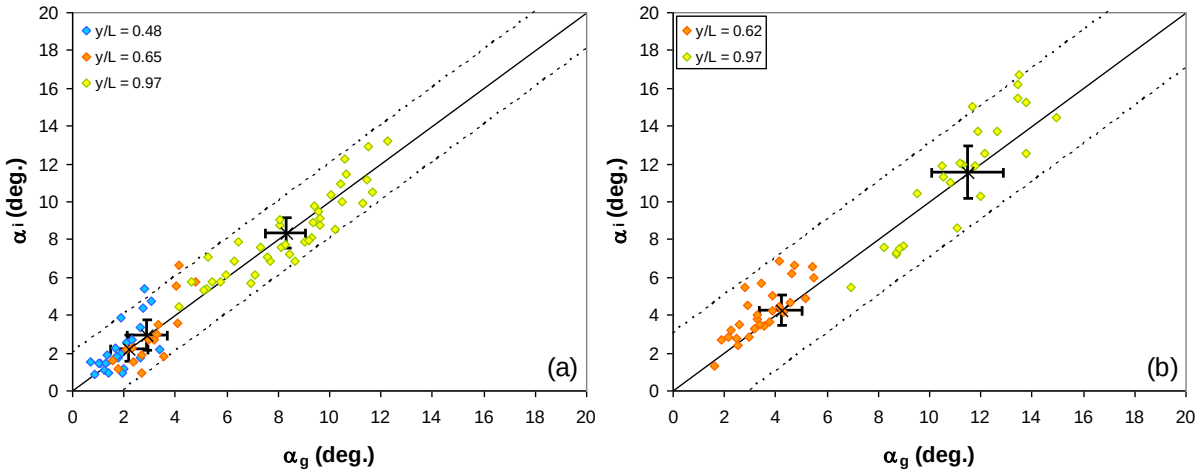

Figure 9

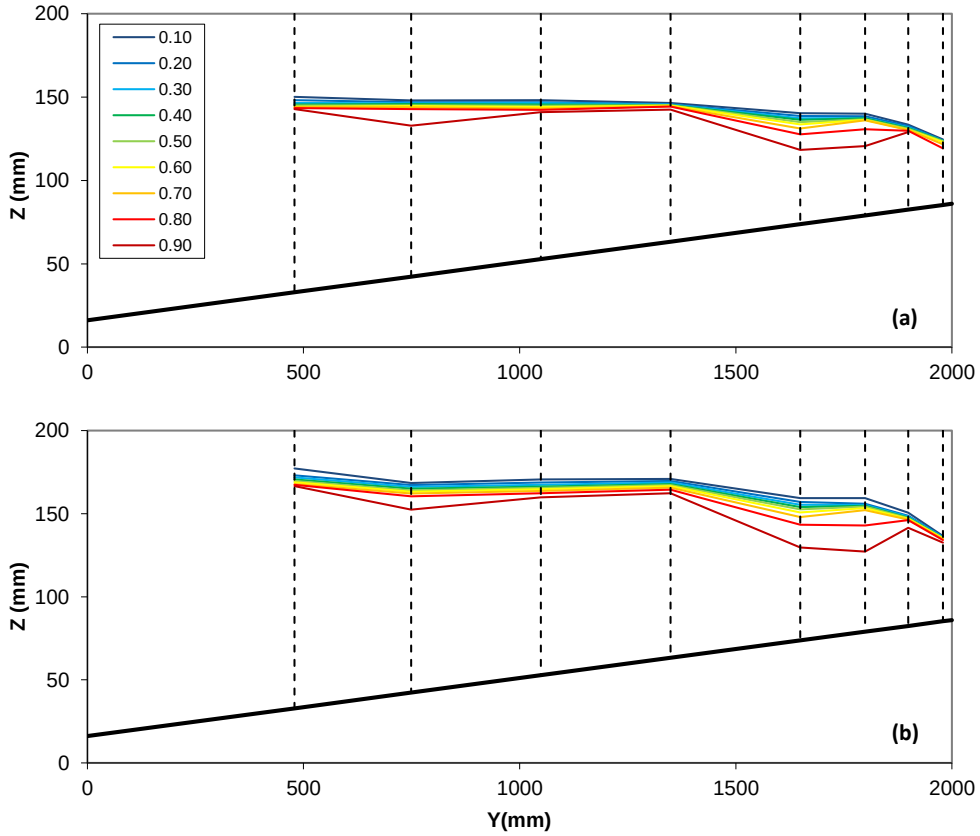
0.10
0.20
0.30
0.40
0.50
0.60
0.70
0.80
0.90
Z (mm)
200
150
100
50
0
0
500
1000
1500
2000
(a)
Z (mm)
200
150
100
50
0
0
500
1000
1500
2000
Y(mm)
(b)

Figure 10

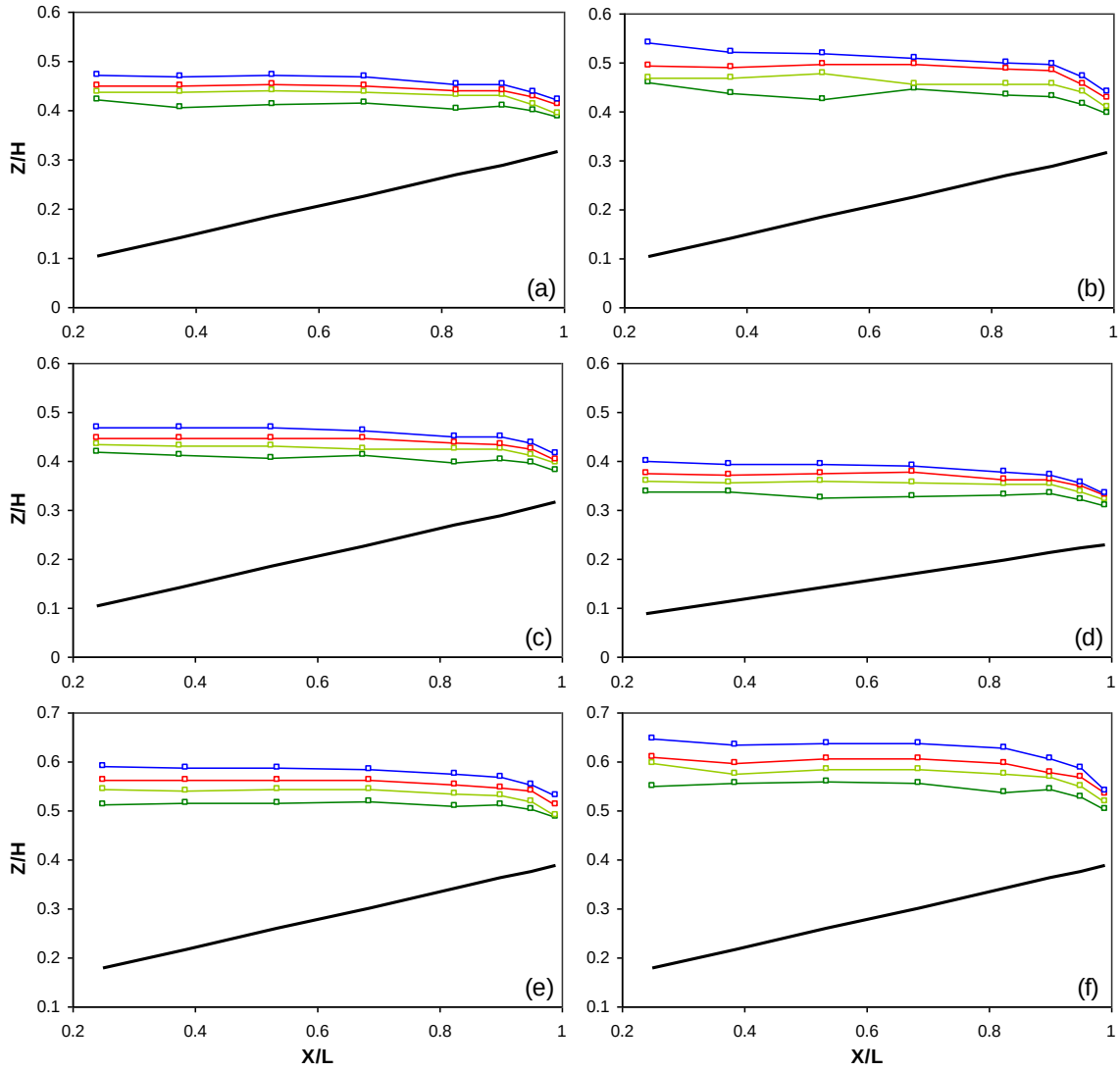

Figure 11

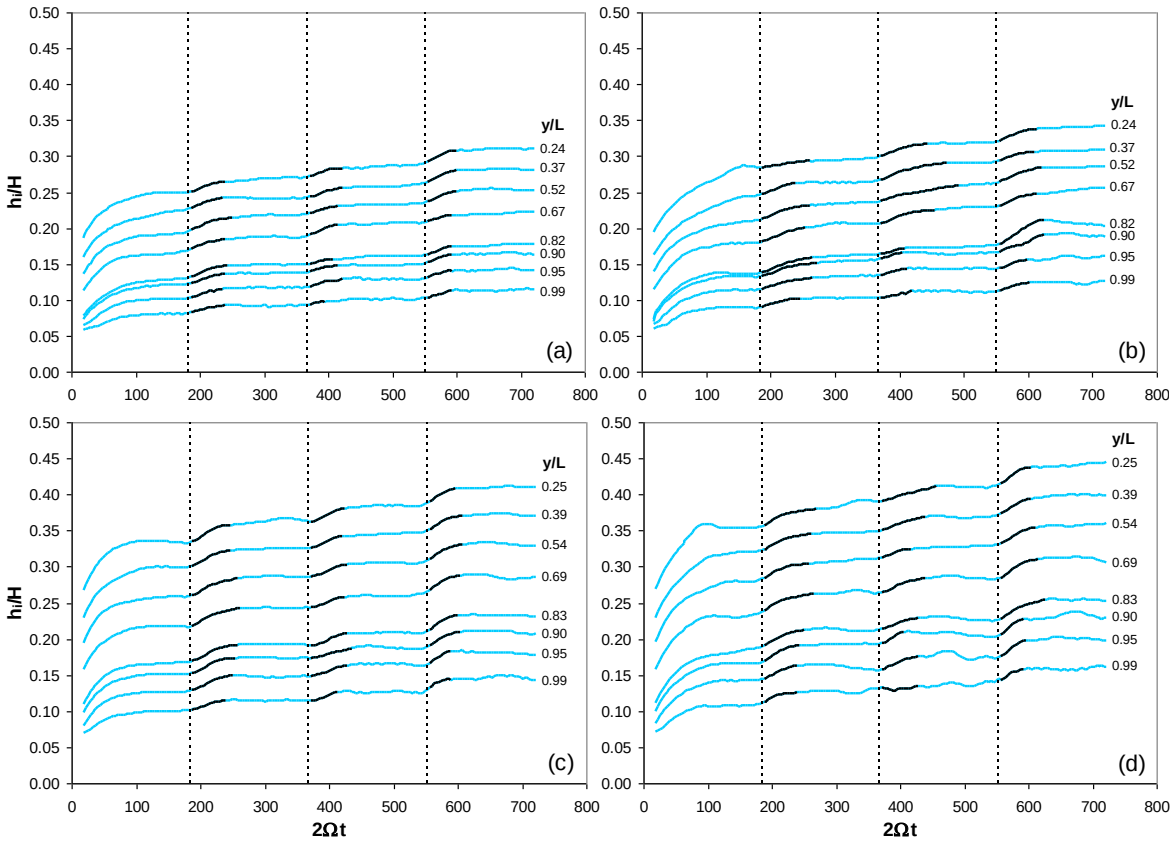
hi/H
2Ωt
y/L
0.24
0.37
0.52
0.67
0.82
0.90
0.95
0.99
(a)
(b)
y/L
0.25
0.39
0.54
0.69
0.83
0.90
0.95
0.99
(c)
(d)

Figure 12

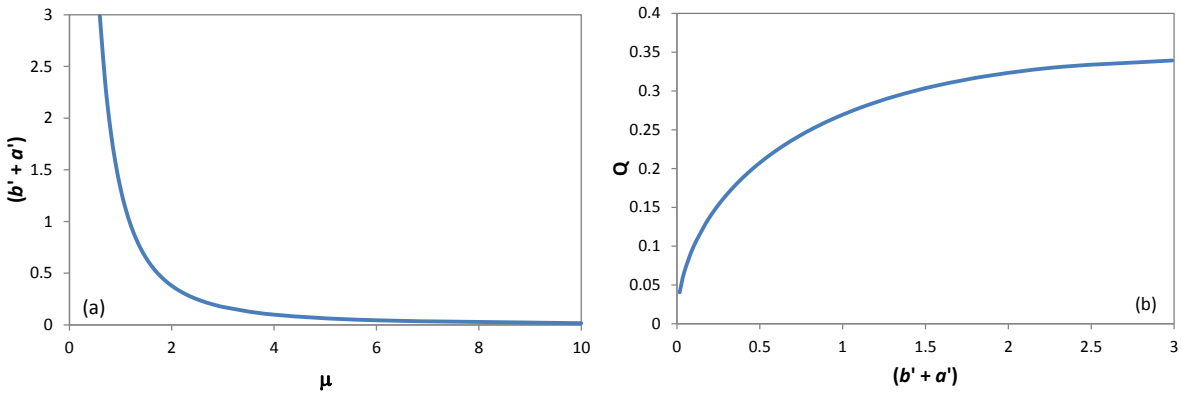
3
2.5
2
1.5
1
0.5
0
(b' + a')
(a)
0
2
4
6
8
10
μ
0.4
0.35
0.3
0.25
0.2
0.15
0.1
0.05
0
Q
(b)
0
0.5
1
1.5
2
2.5
3
(b' + a')

Figure 13

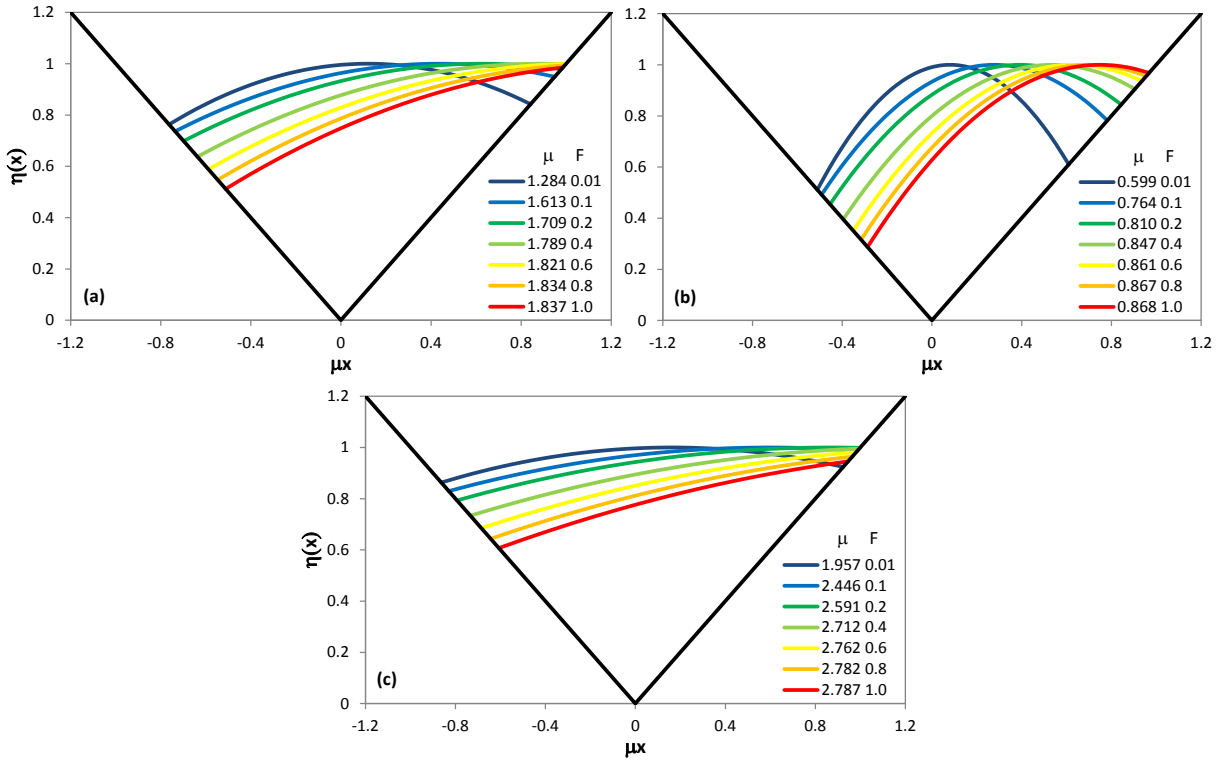
η(x)
μx
(a)
μ F
1.284 0.01
1.613 0.1
1.709 0.2
1.789 0.4
1.821 0.6
1.834 0.8
1.837 1.0
(b)
μ F
0.599 0.01
0.764 0.1
0.810 0.2
0.847 0.4
0.861 0.6
0.867 0.8
0.868 1.0
(c)
μ F
1.957 0.01
2.446 0.1
2.591 0.2
2.712 0.4
2.762 0.6
2.782 0.8
2.787 1.0

Figure 14

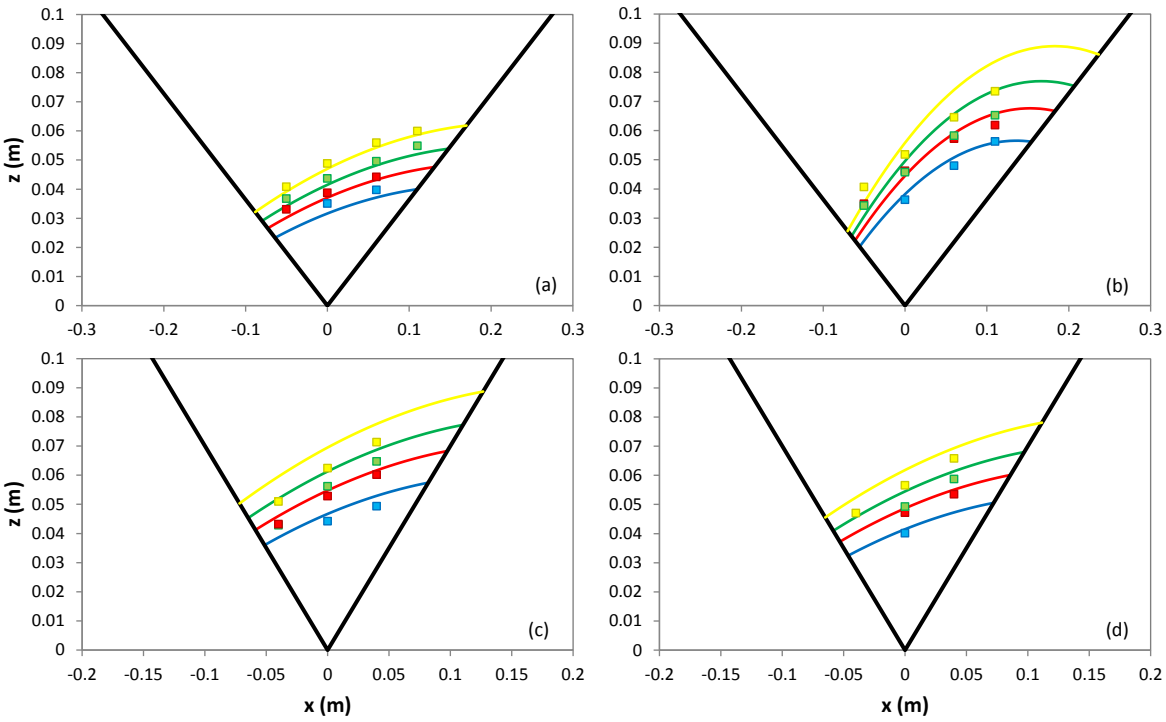

Figure 15

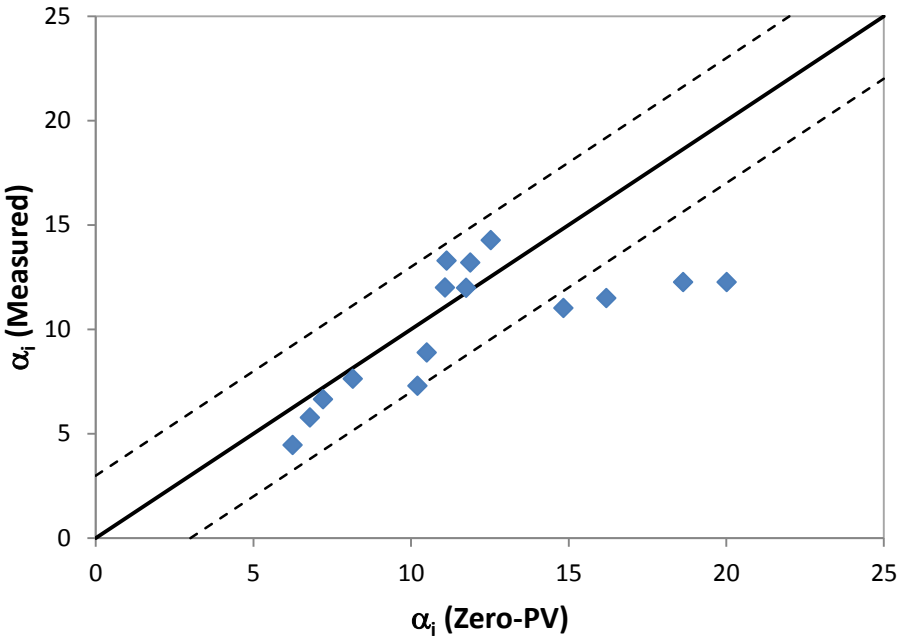

Figure 16

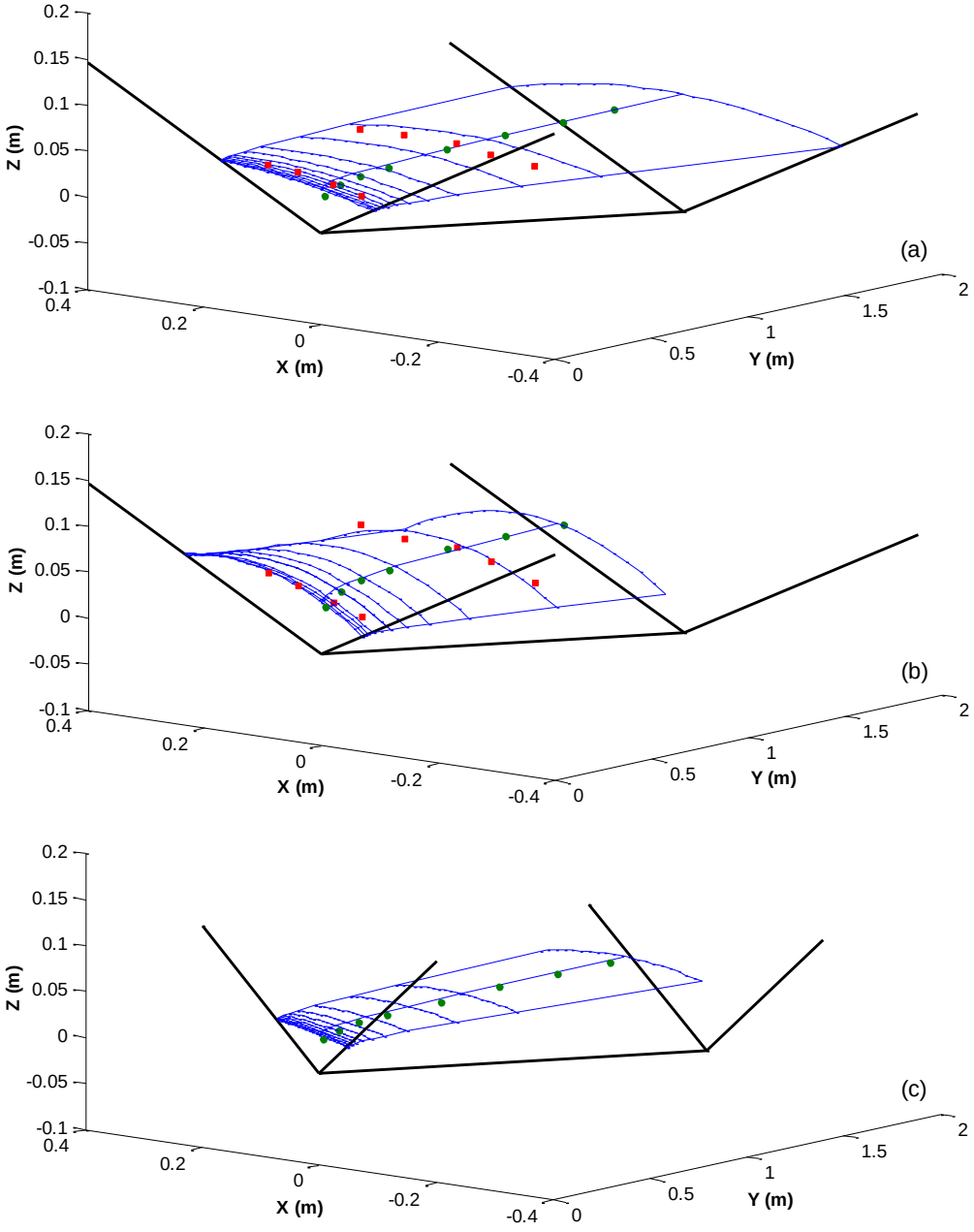

Figure 17

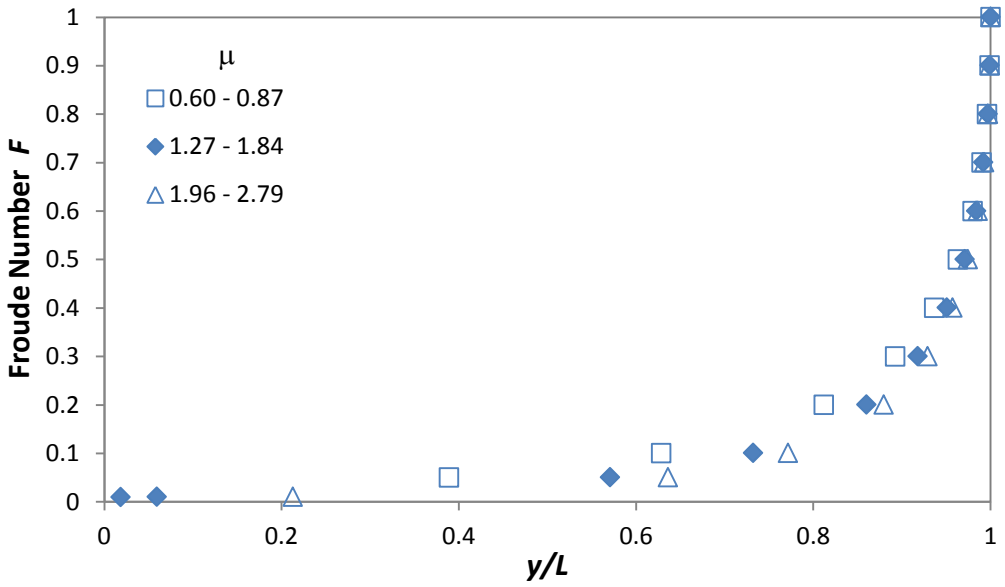
Froude Number F
y/L
μ
0.60 - 0.87
1.27 - 1.84
1.96 - 2.79
0
0.1
0.2
0.3
0.4
0.5
0.6
0.7
0.8
0.9
1
0
0.2
0.4
0.6
0.8
1

Figure 18